



Missouri University of Science and Technology
Scholars' Mine

Mechanical and Aerospace Engineering Faculty
Research & Creative Works

Mechanical and Aerospace Engineering

01 Mar 2010

Three-Dimensional Modeling of Transport Phenomena and their Effect on the Formation of Ripples in Gas Metal Arc Welding

Z. H. Rao

J. Zhou

S. M. Liao

Hai-Lung Tsai

Missouri University of Science and Technology, tsai@mst.edu

Follow this and additional works at: https://scholarsmine.mst.edu/mec_aereng_facwork

 Part of the [Aerospace Engineering Commons](#), and the [Mechanical Engineering Commons](#)

Recommended Citation

Z. H. Rao et al., "Three-Dimensional Modeling of Transport Phenomena and their Effect on the Formation of Ripples in Gas Metal Arc Welding," *Journal of Applied Physics*, vol. 107, American Institute of Physics (AIP), Mar 2010.

The definitive version is available at <https://doi.org/10.1063/1.3326163>

This Article - Journal is brought to you for free and open access by Scholars' Mine. It has been accepted for inclusion in Mechanical and Aerospace Engineering Faculty Research & Creative Works by an authorized administrator of Scholars' Mine. This work is protected by U. S. Copyright Law. Unauthorized use including reproduction for redistribution requires the permission of the copyright holder. For more information, please contact scholarsmine@mst.edu.

Three-dimensional modeling of transport phenomena and their effect on the formation of ripples in gas metal arc welding

Z. H. Rao,^{1,2} J. Zhou,³ S. M. Liao,¹ and H. L. Tsai^{2,a)}

¹*School of Energy Science and Engineering, Central South University, Changsha 410083, China*

²*Department of Mechanical and Aerospace Engineering, Missouri University of Science and Technology, Rolla, Missouri 65409, USA*

³*Department of Mechanical Engineering, The Pennsylvania State University Erie, The Behrend College, 1501 Jordan Road, Erie, Pennsylvania 16563, USA*

(Received 23 October 2009; accepted 18 January 2010; published online 10 March 2010)

Distinct, periodic arc-shaped ripples are observed on the surface of the weld bead in almost any welded components which have a significant effect on weld quality. This article presents the complex transport phenomena and their effect on the formation of ripples in three-dimensional moving gas metal arc welding. The transient distributions of the melt flow velocity and temperature in the weld pool, weld pool shape and dynamics, and solidified weld bead are calculated. It is found that the surface ripples are formed by the interplay between the up-and-down weld pool dynamics, caused mainly by the periodic droplet impingements, and the rate of weld pool solidification. The effects of various welding parameters, including the welding current, droplet size, droplet frequency, droplet impinging velocity, and travel speed on the pitch (distance between two ripples) and height of the ripple are investigated. This study provides fundamental understanding to the underlying physics that cause the formation of ripples with different pitches and heights.

© 2010 American Institute of Physics. [doi:10.1063/1.3326163]

I. INTRODUCTION

Gas metal arc welding (GMAW) has been widely employed for jointing metals due to its high productivity, low costs, and simple to use. However, GMAW involves very complex transport phenomena, including the arc plasma, the melting of electrode, metal transfer, and weld pool dynamics. With the increasing requirement of mechanization and automation, the selection of optimum operating parameters for GMAW becomes essential for high weld quality and productivity. One of the critical measures for assessing overall weld quality is the weld bead profile, which has direct influences on the stresses in the welded-structure, weld joint strength, and fatigue life. Weld ripples are of rather distinct, periodic arc-shaped topographic features on a solidified weld bead surface, which is slightly higher than the surface. Surface rippling is more than a surface phenomenon and is generally associated with segregation, porosity, and other microstructural defects.¹

To date, only a few studies on gas tungsten arc welding (GTAW) or GMAW have been focused on the fundamental understanding of possible mechanisms that lead to the formation of surface ripples.²⁻⁶ It has been found that the formation of ripples is complex and probably involves more than one mechanism, depending on the process variables. The possible causes for surface rippling include: (1) Marangoni or thermocapillary force; (2) periodic weld pool oscillations during solidification; (3) power-source ripples; and (4) periodic swellings of liquid metal.² For GTAW and GMAW, the ripple formation is generally attributed to the weld pool solidification while it is oscillating. In GTAW, arc

plasma exerts a sufficient pressure on the weld pool surface to produce pool oscillations when the arc plasma pressure either fluctuates or is released.³⁻⁵ A great deal of research on the weld pool oscillation in GTAW has been carried out experimentally and theoretically.⁷⁻¹¹ The GMAW process is much more complex than the GTAW process because GMAW involves the impingement of droplets onto the weld pool, producing the periodical mixing of mass, momentum, thermal energy, and species in the weld pool. Some researchers^{6,12-15} studied the GMAW weld pool dynamics by considering the moving arc and the droplet impingement but very few of them⁶ specifically included surface rippling. During the GMAW process, the ripple formation mainly involves the liquid surface oscillation near the tail edge of the weld pool caused by the droplet impinging momentum. Hence, surface rippling in GMAW would be affected by several welding parameters, including the welding power (current and voltage), electrode diameter, wire feed speed, travel speed, and the interplay between these process parameters. Note the welding current, electrode diameter, and wire feed speed affect the electrode melting, droplet generation, and metal transfer, which in turn produce a variety of droplet sizes, droplet frequencies, and droplet impinging velocities onto the weld pool.

GMAW involves nontransparent metal and high temperature plasma, and all welding parameters are coupled in a transient manner. Hence, it is rather difficult to experimentally quantify the effect of each parameter and identify its importance. Mathematical modeling certainly provides an effective means to resolve this problem. Numerous models have been developed to simulate the two-dimensional (2D) stationary GMAW process¹⁶⁻²⁷ and three-dimensional (3D) moving GMAW.^{6,28-31} Tsao and Wu¹⁶ and Jaidi and Dutta¹⁷

^{a)}Electronic mail: tsai@mst.edu. FAX: +1-573-341-4607.

numerically studied the 2D weld pool convection but they assumed the weld pool surface is flat and metal transfer was ignored. Wang and Tsai^{18–20} and Fan and Kovacevic^{21,22} presented 2D mathematical models to predict the weld pool dynamics and weld bead profiles with free surface, including the periodic impingement of droplets onto the weld pool and the solidification process. Zhu *et al.*²³ and Hu and Tsai^{24,25} further developed a comprehensive 2D GMAW model, capable of simulating the interactive coupling between the arc plasma; melting of the electrode; droplet formation, detachment, transfer, and impingement onto the workpiece; and weld pool dynamics. The comprehensive model was further used to study the effect of welding current on the droplet generation and metal transfer in the arc.^{26,27} For 3D moving GMAW, a simultaneous process involving the melting of the new solid base metal ahead of the molten pool and the solidification behind the weld pool leads to more complicated transport phenomena. There are a few articles^{12–15} on the modeling of 3D moving GMAW. Using boundary-fitted coordinates, Kim and Na¹² presented a 3D quasisteady heat and fluid flow analysis for the moving heat source of GMAW with free surface. However, in their model, the impingement of droplets, the depression of weld pool surface by arc pressure, and Marangoni force were ignored. Ushio and Wu¹³ calculated the 3D GMAW weld reinforcement and weld pool surface deformation by adopting a boundary-fitted nonorthogonal coordinate system. But the fluid flow and temperature fields were assumed to be steady state in their model. Ohring and Lugt¹⁴ developed a transient 3D GMAW weld pool model by incorporating the droplet and moving arc effects. However, the impacting liquid metal onto the weld pool is modeled as a liquid column with constant vertical speed acting directly under the welding arc center, which is not consistent with the periodic droplet impingement in reality. Cao *et al.*¹⁵ used a commercial software package, FLOW-3D, to simulate a transient moving weld pool with free surface and droplet impingement but the droplet generation was not included in their calculation. Hu *et al.*⁶ developed a transient moving 3D GMAW model and explained the formation of ripples. However, their work did not consider the effects of various welding parameters on the formation of ripples.

From the above review, it is clear that so far the experimental or numerical investigation on the surface rippling in GMAW is very limited. The role that each welding parameter plays on the surface rippling has not been well understood. In this paper, a 3D moving GMAW model employing the volume of fluid (VOF) technique²⁸ and the continuum formulation²⁹ is developed to simulate the fluid flow and heat transfer in the weld pool. The emphasis is placed on the formation of ripple under various welding conditions. Although the transient arc plasma and droplet formation have been calculated in our previous models,^{24–27} in this study they are not included due to the consideration of excess computational time. Instead, the results directly from experiments³⁰ and modeling²⁷ are used in the present study, including the welding current, droplet size, droplet frequency, and droplet impinging velocity. Note these welding parameters are coupled in a transient manner, and the droplet size and droplet frequency are also closely related to the

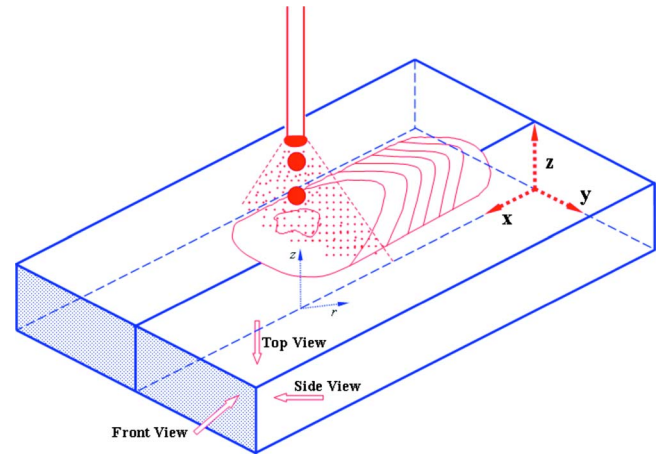


FIG. 1. (Color online) Schematic sketch of a 3D moving GMAW system; x - y - z is a fixed coordinate system and r - z is a local coordinate system moving along with the arc center.

electrode diameter and wire feed speed in practice. The major assumptions in this study include a perfect spherical shape of the droplet and a perfect Gaussian distribution of the arc heat and the arc pressure. These assumptions in general will not alter the underlying physics for the formation of ripples. This work provides a fundamental understanding to the mechanism of ripple formation which may be helpful for controlling welding conditions to reduce ripples on the weld bead.

II. MATHEMATICAL MODEL

A. Governing equations

Figure 1 is a schematic sketch of a moving GMAW on a plain plate. The 3D x - y - z coordinate system is fixed to the stationary base metal, while a 2D r - z cylindrical coordinate system is moving with the arc center. In GMAW, in addition to the thermal energy, mass, and momentum carried by the droplet, the arc heat flux and arc pressure are simultaneously impacting on the base metal. In this study, droplets at a given temperature are assumed to periodically impinge onto the base metal in the negative z -direction, while moving at the same velocity as the arc along the x -direction. Once a droplet reaches the workpiece, the mass, momentum, energy, and species carried by the droplet immerse into the weld pool, which are immediately considered to be part of the base metal. The mathematical formulation given below is valid for both the base metal and the droplet. The partial differential equations governing the conservation of mass, momentum, energy, and species based on the continuum formulation developed by Diao and Tsai²⁹ are modified and employed in the present study and are given below.

(1) Continuity

$$\frac{\partial}{\partial t}(\rho) + \nabla(\rho\mathbf{V}) = 0. \quad (1)$$

(2) Momentum

$$\begin{aligned}
& \frac{\partial}{\partial t}(\rho u) + \nabla \cdot (\rho \mathbf{V}u) \\
&= \nabla \cdot \left(\mu_l \frac{\rho}{\rho_l} \nabla u \right) - \frac{\partial p}{\partial x} - \frac{\mu_l \rho}{K \rho_l} (u - u_s) \\
& - \frac{C\rho^2}{K^{1/2} \rho_l} |u - u_s| (u - u_s) - \nabla \cdot (\rho f_s f_l \mathbf{V}_r u_r) \\
& + \nabla \cdot \left[\mu_l u \nabla \left(\frac{\rho}{\rho_l} \right) \right] + \mathbf{J} \times \mathbf{B}|_x, \quad (2)
\end{aligned}$$

$$\begin{aligned}
& \frac{\partial}{\partial t}(\rho v) + \nabla \cdot (\rho \mathbf{V}v) \\
&= \nabla \cdot \left(\mu_l \frac{\rho}{\rho_l} \nabla v \right) - \frac{\partial p}{\partial y} - \frac{\mu_l \rho}{K \rho_l} (v - v_s) \\
& - \frac{C\rho^2}{K^{1/2} \rho_l} |v - v_s| (v - v_s) - \nabla \cdot (\rho f_s f_l \mathbf{V}_r v_r) \\
& + \nabla \cdot \left[\mu_l v \nabla \left(\frac{\rho}{\rho_l} \right) \right] + \mathbf{J} \times \mathbf{B}|_y, \quad (3)
\end{aligned}$$

$$\begin{aligned}
& \frac{\partial}{\partial t}(\rho w) + \nabla \cdot (\rho \mathbf{V}w) = \rho g + \nabla \cdot \left(\mu_l \frac{\rho}{\rho_l} \nabla w \right) - \frac{\partial p}{\partial z} \\
& - \frac{\mu_l \rho}{K \rho_l} (w - w_s) - \frac{C\rho^2}{K^{1/2} \rho_l} |w - w_s| \\
& \times (w - w_s) - \nabla \cdot (\rho f_s f_l \mathbf{V}_r w_r) \\
& + \nabla \cdot \left[\mu_l w \nabla \left(\frac{\rho}{\rho_l} \right) \right] + \rho g [\beta_T (T \\
& - T_0) + \beta_s (f_l^\alpha - f_{l,0}^\alpha)] + \mathbf{J} \times \mathbf{B}|_z. \quad (4)
\end{aligned}$$

(3) Energy

$$\begin{aligned}
& \frac{\partial}{\partial t}(\rho h) + \nabla \cdot (\rho \mathbf{V}h) = \nabla \cdot \left(\frac{k}{c_s} \nabla h \right) + \nabla \cdot \left[\frac{k}{c_s} \nabla (h_s - h) \right] \\
& - \nabla \cdot [\rho (\mathbf{V} - \mathbf{V}_s)(h_l - h)]. \quad (5)
\end{aligned}$$

(4) Species

$$\begin{aligned}
& \frac{\partial}{\partial t}(\rho f^\alpha) + \nabla \cdot (\rho \mathbf{V}f^\alpha) = \nabla \cdot (\rho D \nabla f^\alpha) + \nabla \\
& \cdot [\rho D \nabla (f_l^\alpha - f^\alpha)] - \nabla \cdot [\rho (\mathbf{V} - \mathbf{V}_s) \\
& \times (f_l^\alpha - f^\alpha)]. \quad (6)
\end{aligned}$$

The above equations are used to determine the basic physical parameters in the base metal, including the pressure p , velocities in x -, y -, and z -directions u , v , and w , temperature T , and sulfur concentration f^α . The input material properties include the metal density ρ , viscosity μ , specific heat c , thermal conductivity k , mass diffusion coefficient D , mass fraction f , permeability function K , enthalpy h , and inertial coefficient C . \mathbf{V} is the velocity vector; \mathbf{V}_r is relative velocity vector $\mathbf{V}_l - \mathbf{V}_s$; \mathbf{J} is the electric current density vector; \mathbf{B} is the

magnetic flux vector; β_s and β_T are, respectively, the solutal expansion coefficient and thermal expansion coefficient; the subscripts l , s refer to the liquid phase and solid phase, respectively, and the subscript r means relative to solid phase velocity. The equations are similar to those given in Ref. 29, except the electromagnetic force which is discussed below. As the assumptions to derive the above equations and the physical meaning of their terms are given by Diao and Tsai,²⁹ they will not be repeated here. Note the species equation is included and sulfur is selected in this study. Sulfur is one of the major constituents in steels and is considered to be a surface active element that can have a significant effect on the surface-tension-driven (Marangoni) flow in welding.^{18,20} In addition, the inclusion of species equation allows us to study the mixing phenomena between the base metal and the droplet.

In Eqs. (1)–(6), the continuum density, specific heat, thermal conductivity, mass diffusivity, solid mass fraction, liquid mass fraction, velocity, enthalpy, and mass fraction of constitute are defined as follows:

$$\rho = g_s \rho_s + g_l \rho_l; \quad c = f_s c_s + f_l c_l; \quad k = g_s k_s + g_l k_l,$$

$$D = f_s D_s + f_l D_l; \quad f_s = \frac{g_s \rho_s}{\rho}; \quad f_l = \frac{g_l \rho_l}{\rho},$$

$$\mathbf{V} = f_s \mathbf{V}_s + f_l \mathbf{V}_l; \quad h = h_s f_s + h_l f_l; \quad f^\alpha = f_s f_s^\alpha + f_l f_l^\alpha, \quad (7)$$

where g_s and g_l are the volume fractions of the solid and liquid phases, respectively. If the phase specific heats are assumed constant, the phase enthalpy for the solid and the liquid can be expressed as

$$h_s = c_s T; \quad h_l = c_l T + (c_s - c_l) T_s + H, \quad (8)$$

where H is the latent heat of fusion of the metal.

The assumption of permeability function in the mushy zone requires the consideration of the growth morphology specific to the alloy under study. In the present study, the permeability function analogous to fluid flow in porous media is assumed employing the Carman–Kozeny equation^{31,32}

$$K = \frac{g_l^3}{c_1 (1 - g_l)^2}; \quad c_1 = \frac{180}{d^2}, \quad (9)$$

where d is proportional to the dendrite dimension, which is assumed to be a constant and is on the order of 10^{-2} cm. The inertial coefficient, C , can be calculated from³³

$$C = 0.13 g_l^{-3/2}. \quad (10)$$

B. Tracking of solid–liquid interface

The solid–liquid phase-change is handled by the continuum formulation.²⁹ The third, fourth, and fifth terms in the right-hand-side (RHS) of Eqs. (2) and (3), and similar terms in Eq. (4), vanish at the solid region because $u = u_s = v = v_s = w = w_s = 0$ and $f_l = 0$ for the solid phase. For the liquid region, since K goes to infinity due to $g_l = 1$ in Eq. (9) and $f_s = 0$, all of these terms also vanish. These terms are only valid in the mush zone, where $0 < f_l < 1$ and $0 < f_s < 1$. Therefore, the liquid region, mushy zone, and solid region can be

handled by the same equations. Also, in GMAW, as the arc heat flux is rather concentrated and the solidification time is very short (as compared to casting), it is expected that the mushy zone in the base metal is very small (to be proved later), and the solid phase velocity is assumed to be zero in the mushy zone. During the fusion and solidification process, latent heat is absorbed or released in the mushy zone. By using the enthalpy, conduction in the solid region, conduction and convection in the liquid region, and mushy zone, the absorption and release of latent heat are all handled by the same equation, Eq. (5).

C. Tracking of free surface

The algorithm of VOF is used to track the dynamic geometry of the free surface.²⁸ The fluid configuration is defined by a VOF function, $F(x, y, z, t)$, which tracks the location of the free surface. This function represents the VOF per unit volume and satisfies the following conservation equation:

$$\frac{dF}{dt} = \frac{\partial F}{\partial t} + (\mathbf{V} \cdot \nabla)F = 0. \quad (11)$$

When averaged over the cells of a computing mesh, the average value of F in a cell is equal to the fractional volume of the cell occupied by the fluid. A unit value of F corresponds to a cell full of fluid; whereas, a zero value indicates a cell containing no fluid. Cells with F values between zero and one are partially filled with fluid and identified as surface cells.

D. Boundary conditions

The boundary conditions for the solution of Eqs. (1)–(6) are given below.

1. Normal to the local free surface

For cells containing free surface, that is, cells that contain fluid but have one or more empty neighbors, the following pressure conditions must be satisfied:²⁸

$$p = p_v + \gamma\kappa, \quad (12)$$

where p is the pressure at the free surface in a direction normal to the local free surface and p_v is the vapor pressure or any other applied external pressure acting on the free surface, which, in the present study, is the plasma arc pressure. The plasma arc pressure is assumed to have a radial distribution in the following form:¹³

$$p_v = P_{\max} \exp\left(-\frac{r^2}{2\sigma_p^2}\right), \quad (13)$$

where P_{\max} is the maximum arc pressure at the arc center ($x=x_a$, $y=0$), r is the distance from the arc center, and σ_p is the arc pressure distribution parameter. In Eq. (12), κ is the free surface curvature given by²⁸

$$\kappa = -\left[\nabla \cdot \left(\frac{\vec{n}}{|\vec{n}|}\right)\right] = \frac{1}{|\vec{n}|} \left[\left(\frac{\vec{n}}{|\vec{n}|} \cdot \nabla\right)|\vec{n}| - (\nabla \cdot \vec{n}) \right], \quad (14)$$

where \vec{n} is a normal vector to the local surface, which is the gradient of VOF function

$$\vec{n} = \nabla F. \quad (15)$$

2. Tangential to the local free surface

The temperature and sulfur concentration dependent Marangoni shear stress at the free surface in a direction tangential to the local free surface is given by

$$\tau_s = \mu_l \frac{\partial(\mathbf{V} \cdot \vec{s})}{\partial \vec{n}} = \frac{\partial \gamma}{\partial T} \frac{\partial T}{\partial \vec{s}} + \frac{\partial \gamma}{\partial f^\alpha} \frac{\partial f^\alpha}{\partial \vec{s}}, \quad (16)$$

where \vec{s} is a tangential vector to the local surface. Surface tension γ for a pseudobinary Fe–S system as a function of temperature, T , and sulfur concentration, f^α is given by³⁴

$$\gamma = 1.943 - 4.3 \times 10^{-4}(T - 1723) - RT \times 1.3 \times 10^{-8} \ln\left[1 + 0.00318f^\alpha \exp\left(\frac{1.66 \times 10^8}{RT}\right)\right], \quad (17)$$

where R is the gas constant. Note the surface tension and its gradients as a function of temperature and sulfur concentration for the pseudobinary Fe–S system are plotted in Ref. 20.

3. Top surface

At the moving arc center, in addition to the droplet impingement, arc heat flux is also impacting on the base metal. As arc heat flux is relatively concentrated, it is assumed that the heat flux is perpendicular to the base metal (i.e., neglecting the inclination nature of current and heat flux). Hence, the temperature and concentration boundary conditions at the top surface of the base metal are

$$k = \frac{\partial T}{\partial z} = \frac{\eta(1 - \eta_d)Iu_w}{2\pi\sigma_q^2} \exp\left(-\frac{r^2}{2\sigma_q^2}\right) - q_{\text{conv}} - q_{\text{radi}} - q_{\text{evap}}, \quad (18)$$

$$\frac{\partial f^\alpha}{\partial z} = 0, \quad (19)$$

where I is the welding current, η is the arc thermal efficiency, η_d is the ratio of droplet thermal energy to the total arc energy, u_w is the arc voltage, and σ_q is the arc heat flux distribution parameter. The heat loss due to convection, radiation, and evaporation can be written as

$$q_{\text{conv}} = h_c(T - T_\infty); \quad q_{\text{radi}} = \sigma\varepsilon(T^4 - T_\infty^4); \quad q_{\text{evap}} = WH_v, \quad (20)$$

where h_c is the convective heat transfer coefficient, T_∞ is the ambient temperature, H_v is the latent heat for liquid-vapor phase-change, σ is the Stefan–Boltzmann constant, ε is the radiation emissivity, and W is the melt mass evaporation rate. For a metal such as steel, W can be written as³⁵

$$\log(W) = A_v + \log P_{\text{atm}} - 0.5 \log T, \quad (21)$$

$$\log P_{\text{atm}} = 6.121 - \frac{18\,836}{T}. \quad (22)$$

4. Symmetrical $y=0$ plane

$$\frac{\partial T}{\partial y} = 0; \quad u = 0; \quad \frac{\partial v}{\partial y} = 0; \quad w = 0; \quad \frac{\partial f^\alpha}{\partial y} = 0. \quad (23)$$

5. Other surfaces

$$-k \frac{\partial T}{\partial \vec{n}} = q_{\text{conv}}; \quad u = 0; \quad v = 0; \quad w = 0; \quad \frac{\partial f^\alpha}{\partial \vec{n}} = 0, \quad (24)$$

where \vec{n} can be x -, y -, or z -direction.

E. Electromagnetic force

In each of the Eqs. (2)–(4), there is a term caused by the electromagnetic force that should be calculated first before the calculation of velocity. Assuming the electric field is quasi-steady state and the electrical conductivity is constant, the scalar electric potential, ϕ , satisfies the following Maxwell equation in the local r - z coordinate system²⁴

$$\nabla^2 \phi = \frac{1}{r} \frac{\partial}{\partial r} \left(r \frac{\partial \phi}{\partial r} \right) + \frac{\partial^2 \phi}{\partial z^2} = 0. \quad (25)$$

Assuming current is in the negative z -direction, the required boundary conditions for the solution of Eq. (25) are

$$-\sigma_e \frac{\partial \phi}{\partial z} = \frac{I}{2\pi\sigma_c^2} \exp\left(-\frac{r^2}{2\sigma_c^2}\right) \quad \text{at the top surface}, \quad (26)$$

$$\frac{\partial \phi}{\partial z} = 0 \quad \text{at} \quad z = 0, \quad (27)$$

$$\frac{\partial \phi}{\partial r} = 0 \quad \text{at} \quad r = 0, \quad (28)$$

$$\phi = 0 \quad \text{at} \quad r = 10\sigma_c, \quad (29)$$

where σ_e is the electrical conductivity and σ_c is the arc current distribution parameter. After the distribution of electrical potential is solved, current density in the r and z -directions can be calculated via

$$J_r = -\sigma_e \frac{\partial \phi}{\partial r}; \quad J_z = -\sigma_e \frac{\partial \phi}{\partial z}. \quad (30)$$

The self-induced azimuthal magnetic field is derived from Ampere's Law through²⁴

$$B_\theta = \frac{\mu_0}{r} \int_0^r J_z r dr, \quad (31)$$

where μ_0 is the magnetic permeability. Finally, the three components of electromagnetic force in Eqs. (2)–(4) are calculated via

$$\mathbf{J} \times \mathbf{B}|_x = -B_\theta J_z \frac{x-x_a}{r}; \quad \mathbf{J} \times \mathbf{B}|_y = -B_\theta J_z \frac{y}{r};$$

$$\mathbf{J} \times \mathbf{B}|_z = B_\theta J_r. \quad (32)$$

III. NUMERICAL CONSIDERATIONS

In the present study, the transport phenomena in the base metal are calculated, and the coupling between the metal domain and the arc plasma is considered through specific boundary conditions on the top surface. Thus, the calculation for arc domain is not included in this study. Finite difference conventions follow that of the MAC (Marker-And-Cell) scheme³⁶ in which x -, y -, and z -velocity components are located at the cell face centers on lines of constant x , y , and z , respectively, and the pressure, VOF function, temperature, and concentration are located at cell centers. The governing differential equations [Eqs. (1)–(6) and (11)] and all related supplemental and boundary conditions are solved through the following iterative scheme:

- (1) At each time step, the current continuity equation, Eq. (25), is solved first based on the updated parameters. The new distributions of current density and electromagnetic force are then calculated for the momentum and energy equations.
- (2) The surface force, such as the arc pressure, surface tension, and Marangoni shear stress, as well as heat flux at the top surface are calculated, and the other boundary conditions, such as that caused by droplet impingement, are evaluated for the momentum and energy equations.
- (3) The method developed by Torrey *et al.*³⁷ is used to solve p , u , v , w , T , and f^α . This method is Eulerian and the basic procedure for advancing the solution through one time step, Δt , consists of three steps. First, at the beginning of the time step, explicit approximations to the momentum Eqs. (2)–(4) are used to find provisional values of the new time velocities. Second, an iterative procedure is used to solve for the pressure and velocity fields that satisfy Eq. (1) to within a convergence criterion at the new time. The energy Eq. (5) and species Eq. (6) are solved and the temperature or species-dependent physical properties are updated.
- (4) Equation (11) is solved to obtain the new free surface profile for the metal domain. The physical properties in the mesh cells and the boundary conditions within the computing domain are updated.
- (5) Advance to the next time step and move the arc center to a new position. Depending upon the droplet frequency and the time, a new droplet with given diameter, temperature, velocity, and concentration may be produced and the surface boundary conditions are imposed on this new droplet. Then, back to step (1) and continue until the desired time is reached.

Since the governing equations are valid in the regions of liquid, solid, and mushy zone, there is no need to track the geometrical shape and the extent of each region. Hence, a fixed-grid system is used in the numerical calculation. A grid system of $610 \times 152 \times 82$ points is utilized for the total computational domain of $300 \times 30 \times 10$ mm³. Due to symmetry of the x - z plane of the domain, only half of the grid points

TABLE I. Thermophysical properties of mild steel and other parameters.

Nomenclature	Symbol	Value (unit)
Constant in Eq. (21)	A_v	2.52
Specific heat of solid phase	c_s	700 (J kg ⁻¹ K ⁻¹)
Specific heat of liquid phase	c_l	780 (J kg ⁻¹ K ⁻¹)
Mass diffusion coefficient of solid phase	D_s	≅0
Mass diffusion coefficient of liquid phase	D_l	3×10^{-5} (cm ² s ⁻¹)
Thermal conductivity of solid phase	k_s	22 (W m ⁻¹ K ⁻¹)
Thermal conductivity of liquid phase	k_l	22 (W m ⁻¹ K ⁻¹)
Density of solid phase	ρ_s	7200 (kg m ⁻³)
Density of liquid phase	ρ_l	7200 (kg m ⁻³)
Thermal expansion coefficient	β_T	4.95×10^{-5} (K ⁻¹)
Solutal expansion coefficient	β_s	-2
Radiation emissivity	ε	0.4
Magnetic permeability	μ_0	1.26×10^{-6} (H m ⁻¹)
Dynamic viscosity	μ_l	0.006 (kg m ⁻¹ s ⁻¹)
Latent heat of fusion	H	2.47×10^5 (J kg ⁻¹)
Latent heat of vaporization	H_v	7.34×10^6 (J kg ⁻¹)
Convective heat transfer coefficient	h_c	100 (W m ⁻² K ⁻¹)
Electrical conductivity	σ_e	7.7×10^5 (Ω^{-1} m ⁻¹)
Solidus temperature	T_s	1750 (K)
Liquidus temperature	T_l	1800 (K)
Reference temperature	T_0	1700 (K)
Ambient temperature	T_∞	300 (K)
Vaporization temperature	T_{ev}	3080 (K)
Arc thermal efficiency	η	80%
Ratio of droplet thermal energy to total arc energy	η_d	48%
Thickness of base metal	H_b	6.0 (mm)
Width of base metal	W_b	30.0 (mm)
Length of base metal	L_b	300.0 (mm)
Initial base metal temperature	T_b	293 (K)
Initial droplet temperature	T_d	2500 (K)
Initial base metal sulfur concentration	f_b^α	100 (ppm)
Electrode wire diameter	d	1.60 (mm)
Initial droplet sulfur concentration	f_d^α	300 (ppm)

(610×76×82) are used in the actual calculation. As the weld pool moves in the welding direction, an adaptive grid system is employed, having finer grids in and near the weld pool. The finer grids concentrating on and around the weld pool move along with the weld pool as the welding proceeds. The average time step is 10^{-4} s and the smallest time step, about 10^{-5} s, occurs when the droplet impinges onto the weld pool.

IV. RESULTS AND DISCUSSION

As shown in Fig. 1, the welding proceeds at a constant speed along the positive x -direction, while spherical droplets at a uniform temperature of 2500 K and with predetermined diameter, frequency, and velocity, periodically impinges onto the base metal in the negative z -direction. Both the workpiece and the droplet are mild steel, and the workpiece is a plate of 30 mm wide, 300 mm long and 6 mm thick. The material properties of the base metal, liquid droplets and other parameters used in the computation are summarized in Table I. The base metal is assumed to contain 100 ppm of sulfur, while the droplet contains 300 ppm. In order to avoid possible end-effect, the welding begins at $x=10.0$ mm and

the time is set as $t=0$ s when the plasma arc is turned on and the first droplet is assumed to generate immediately.

In order to simulate the welding process with realistic conditions, the experimental results³⁰ including droplet size and droplet frequency given in Table II are used as the forced inputs for different welding currents, ranging from 220 to 280 A with an increment of 20 A. The experimental results by Jones *et al.*,³⁰ which are very close to the predicted values by Hu and Tsai,²⁷ were obtained for the welding process with constant welding currents, 1.6 mm mild steel electrode, and shielded by Ar-2% O₂. The shielding gas flow rate was 24 L/min and the inner diameter of the nozzle was 19.1 mm. The droplet impinging velocities in Table II are calculated using the arc length of 8 mm and the measured droplet acceleration in Ref. 30. The corresponding average voltages and other arc heat flux and arc pressure parameters are extracted from the simulated results of Hu and Tsai.²⁷ Unless otherwise specified, the default welding speed is 0.7 cm/s. Although the experimental data, such as droplet size and droplet frequency, and the assumptions, such as spherical droplets and Gaussian distribution of arc pressure, are used in this study, the fundamental physics leading to the formation of ripples should remain the same. For each of the four

TABLE II. The wire feed speeds (Ref. 30), droplet parameters (Ref. 30), and arc parameters (Ref. 27) at different current levels.

Current (A)	220	240	260	280
Electrode wire feed speed (cm/s)	4.3	4.8	5.3	5.8
Droplet diameter, D_d (mm)	2.68	2.34	1.94	1.62
Droplet frequency, D_f (Hz)	8.8	13.8	23.8	59.0
Droplet impinging velocity, D_v (cm/s)	-64.5	-70.0	-92.8	-107.0
Average arc voltage, u_w (V)	15.4	16.9	18.0	19.2
Arc heat flux distribution parameter, σ_q (mm)	2.60	2.67	2.73	2.80
Arc current distribution parameter, σ_c (mm)	2.60	2.67	2.73	2.80
Maximum arc pressure at the arc center, P_{\max} (Pa)	460	540	660	800
Arc pressure distribution parameter, σ_p (mm)	3.0	3.2	3.5	4.0

current levels, the transient distributions of the melt flow velocity, temperature, and sulfur concentration are obtained but only a full set of results for $I=240$ A are presented in Fig. 2 as a typical example to explain the ripple formation process on the weld bead surface.

A. The ripple formation process

Figures 2(a)–2(c) show, respectively, the sequences and the side-view ($y=0$) distributions of velocity, temperature, and sulfur concentration from $t=2.319$ s to 2.410 s, showing

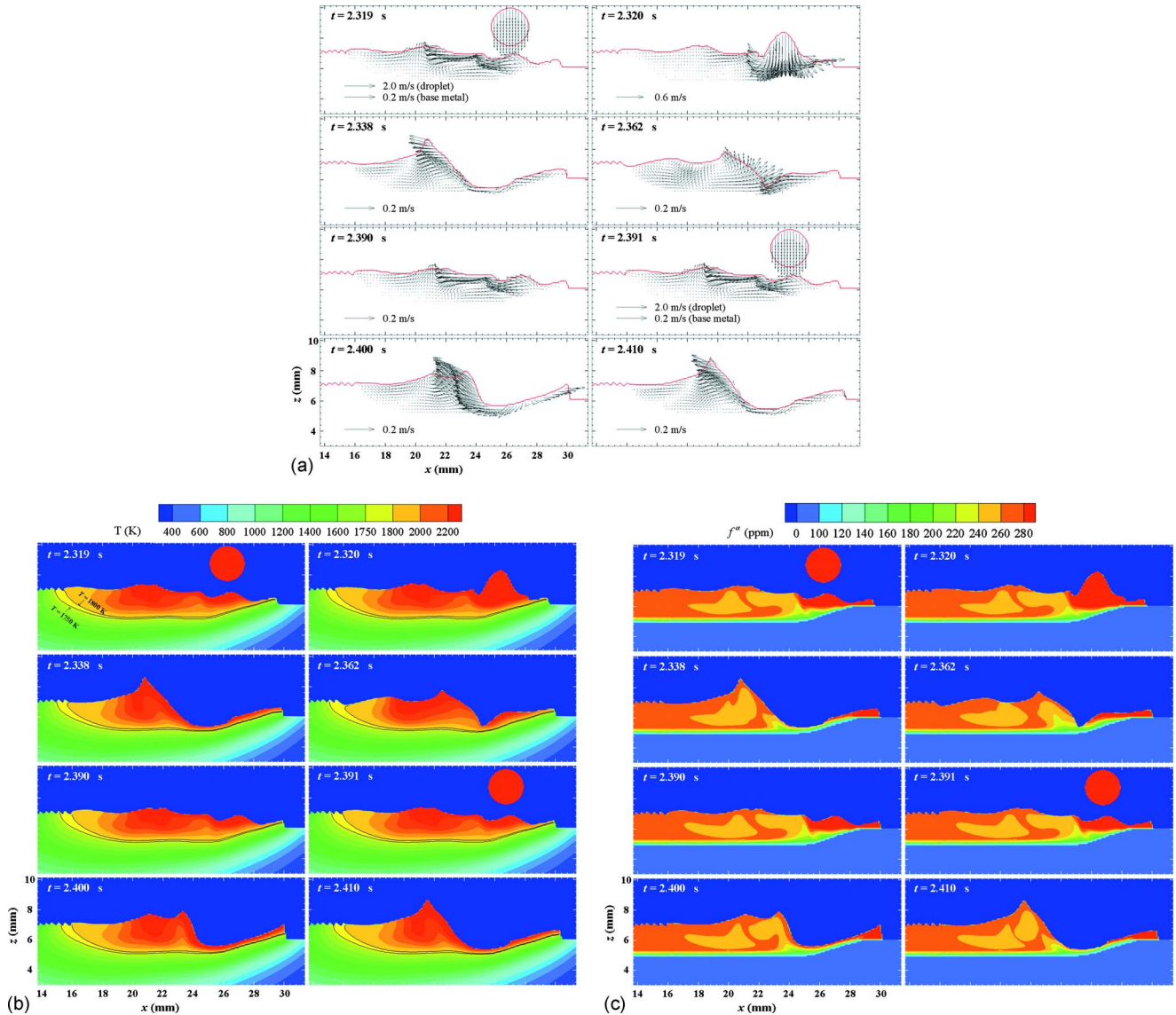


FIG. 2. (Color online) The typical sequences and the distributions of (a) velocity, (b) temperature, and (c) sulfur concentration, showing the formation of ripples (side views, $y=0$); $I=240$ A, $D_d=2.34$ mm, $D_f=13.8$ Hz, $D_v=-70$ cm/s, and $V_a=0.7$ cm/s.

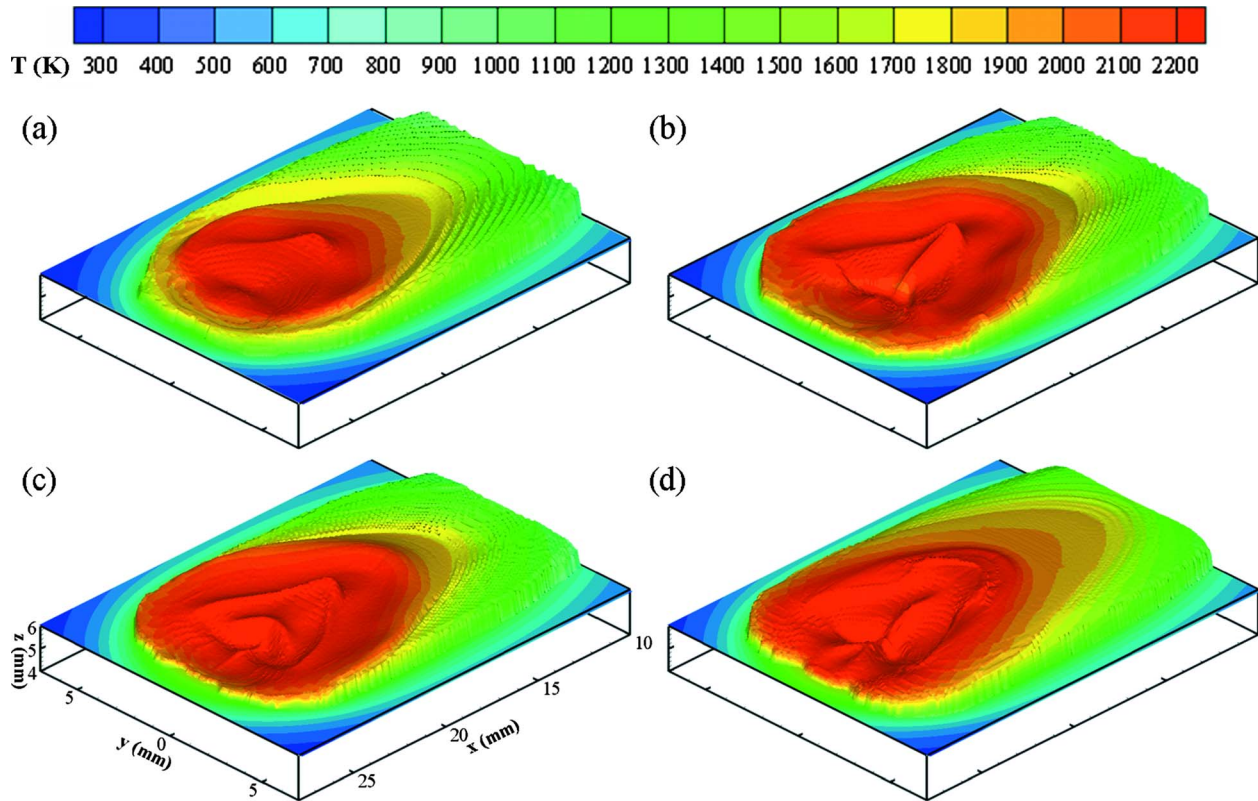


FIG. 3. (Color online) The weld bead shapes with ripples and the 3D temperature distributions at various current levels at $t=2.0$ s: (a) $I=220$ A, (b) $I=240$ A, (c) $I=260$ A, and (d) $I=280$ A; $V_a=0.7$ cm/s, other welding parameters (D_d , D_f , and D_v) vary for different currents and are given in Table II.

the formation process of a ripple. Note the time lags between two subfigures are different. In Fig. 2(a), the top surface of the weld is represented by a solid line; also, in order to increase the readability, only half of the grid nodes are used for plotting the velocity vectors and the velocity scale may be different for the weld pool and the droplet. It is seen at $t=2.319$ s, there are multiple distinct ripples on the surface of the solidified weld bead on the left-hand-side (LHS) of the weld pool. At $t=2.320$ s, a droplet just impinges onto the weld pool and the hot fluid carried by the droplet spreads outward and upward from the arc center. Part of the hot fluid flows forward to the RHS ahead of the arc center which provides heat to melt the “new” workpiece, while on the left, the hot fluid “pushes” the fluid in the weld pool backward to the LHS and thus a crater is created, $t=2.338$ s. As shown at $t=2.362$ s, a “wave shape” of fluid created by the droplet impingement, with higher fluid level in the center and lower fluid level on each side, propagates away from the arc center in the negative x -direction. At the same time, the weld pool solidifies from the tail edge of the weld pool and moves forward in the positive x -direction. The height and width of the wave decrease while it is propagating to the LHS, and eventually “meets” with the solidifying weld. It is seen at $t=2.390$ s the lower level of the fluid on the LHS of the wave is being “frozen” next to the existing “hill” of the ripple and forms the “valley” of a new ripple. The wave continues to propagate to the LHS and the fluid with higher level arrives at the solidified valley and is solidified to become a hill at $t=2.410$ s. After the droplet impinges onto the weld pool at $t=2.391$ s, there is a big surge of the fluid on the LHS. This

big surge tends to draw the fluid from its both sides and lowers the fluid on its LHS. This mechanism helps create the “tip” of the new ripple as shown at $t=2.410$ s.

The fluid flow patterns shown at $t=2.319$ s are almost identical to those at $t=2.391$ s. Similarly, the flow patterns at $t=2.338$ s are very similar to those at $t=2.410$ s. These two sets of subfigures have the same time lags in between which is $\Delta t=0.072$ s (i.e., $2.391-2.319=0.072$ or $2.410-2.338=0.072$). The time lag is consistent with the droplet frequency which is 13.8 Hz (i.e., $1/13.8=0.072$). The same time lags also indicate the welding process and the associated transport phenomena have achieved a cyclical steady state. Note the complex flow pattern in the weld pool is attributed to the combined effect of the arc pressure, droplet impinging force, electromagnetic force, surface tension, and gravity. The arc pressure has a Gaussian distribution that pushes the fluid downward and outward from the arc center; the droplet impinging force produces an outward and upward flow near the arc center; the electromagnetic force is generally downward and inward around the arc center which is determined by the current flow pattern.²⁶ In this study, the temperature-dependent surface tension causes an outward flow from the arc center because the temperature coefficient of surface tension is negative, according to Eq. (17).

The liquidus line ($T=1800$ K) and solidus line ($T=1750$ K) are shown in Fig. 2(b), and the region between them is the mushy zone. It is seen the mushy zone is generally very small which is consistent with our earlier assumption that the solid phase velocity in the mushy zone is zero. Generally, there are two high temperature regions (T

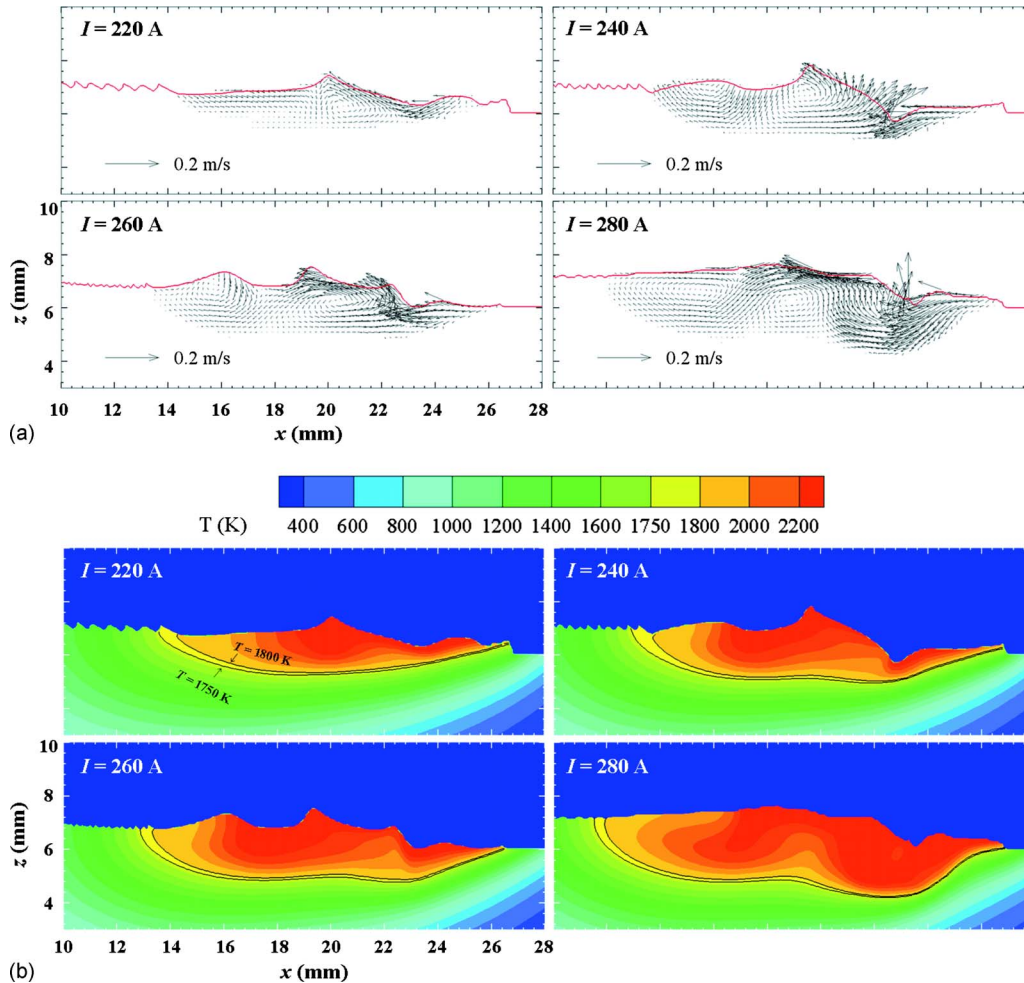


FIG. 4. (Color online) The corresponding side views of (a) velocity distributions and (b) temperature distributions with ripple profiles for the cases as shown in Fig. 3.

> 2200 K) in the weld pool; one is near the arc center that is caused by the arc heating and the thermal energy carried by the droplet, and the other is located at a short distance on the left of the arc center due to the outward flow of the hot droplet fluid.

The aforementioned ripple formation process may be better explained with the help of Fig. 2(b) as there are no velocity vectors and the weld pool shape can be easily seen. At $t=2.319$ s, among the four ripples that have been formed on the LHS of the weld pool, three are fully solidified and one is in the mushy stage, Fig. 2(b). The liquid level of the weld pool next to the ripple (at the temperature higher than the liquidus temperature) is as high as the tip of the ripple, while the solidus line intersects the weld bead surface at the valley between the third and fourth ripple. As the droplet impinges onto the weld pool at $t=2.320$ s, a new crater is created which pushes the fluid in the weld pool upward and away from the arc center (at $t=2.338$ s). It is seen the peak of the weld pool is much higher than the tip of the ripple. The big surge at $t=2.338$ s tends to “bend” the fluid between the surge and the tail edge of the weld pool, which lowers the fluid and the fifth ripple is formed at $t=2.362$ s. Due to gravity and hydrostatic force, the high-level fluid tends to fill

up the crater and decreases the liquid level. Hence, there is an up-and-down motion of the weld pool fluid which generates a “wave” propagating outward in the negative x -direction. As the welding proceeds, the arc and the solidification along with the liquidus and solidus lines move forward in the same x -direction. Note there is a time lag between the droplet impingement and the propagation of the wave to the tail edge.

Figure 2(c) shows the distributions of sulfur concentration in the weld pool which is significantly skewed. The mixing phenomena can be clearly seen between the higher sulfur droplet (300 ppm) and the base metal with a lower sulfur content (100 ppm). There is a high sulfur concentration region near the center of the weld pool which is the result of the upturn of the droplet after impinging onto the weld pool. However, the sulfur concentration in the solidified weld bead is quite uniform which is consistent with the experimental result.¹ The weld penetration or melted depth is about 1 mm below the original workpiece surface.

As described above, the conditions required for the ripple formation include the droplet impingement, the up-and-down movement of the weld pool and the solidification. Therefore, the pitch and height of the ripple are closely re-

TABLE III. The various droplet impinging parameters based on the cases of $I=240$ A.

	Droplet diameter (D_d) (mm)	Droplet frequency (D_f) (Hz)	Droplet impinging velocity (D_v) (cm/s)
Case I	1.6	13.8	-70
Case II	2.6	13.8	-70
Case III	2.34	9	-70
Case IV	2.34	16	-70
Case V	2.34	13.8	-40
Case VI	2.34	13.8	-100

lated to the droplet impinging parameters (droplet size, droplet frequency, and impinging velocity), the weld pool size, and the solidification rate.

B. The effect of welding current

Figure 3 shows the 3D views of temperature distributions and weld pool shapes with ripples for different welding currents. Figure 4 shows the corresponding side views ($y=0$) of the melt flow velocities and temperature contours.

Note the electrode wire feed speed, droplet diameter, droplet frequency, droplet impinging velocity, and average voltage are all coupled with the welding current. In this study, the experimental data³⁰ and the corresponding modeling results,²⁷ given in Table II, are used as the inputs in the simulation. As shown in Table II, as the welding current increases, the droplet diameter decreases, the droplet frequency significantly increases, and the droplet impinging velocity increases. Note at a higher welding current, the power input and the metal deposition rate are higher. As shown in Fig. 3, the distinct ripples can be clearly seen on the surface of the solidified bead at all different current levels. The 3D views show a “standard” tear-drop shape of the weld pool which is consistent with the reported analytical and experimental results.^{12,13} As the welding current increases, the weld pool size and the weld penetration depth increase, as expected. The shape and size of the weld pool are determined by the fluid flow and the dynamic competing between the melting and solidification of the base metal. When the melting is faster than the solidification, the weld pool continuously grows until the solidification rate balances the melting rate. At a higher current level, more intensive arc heating and

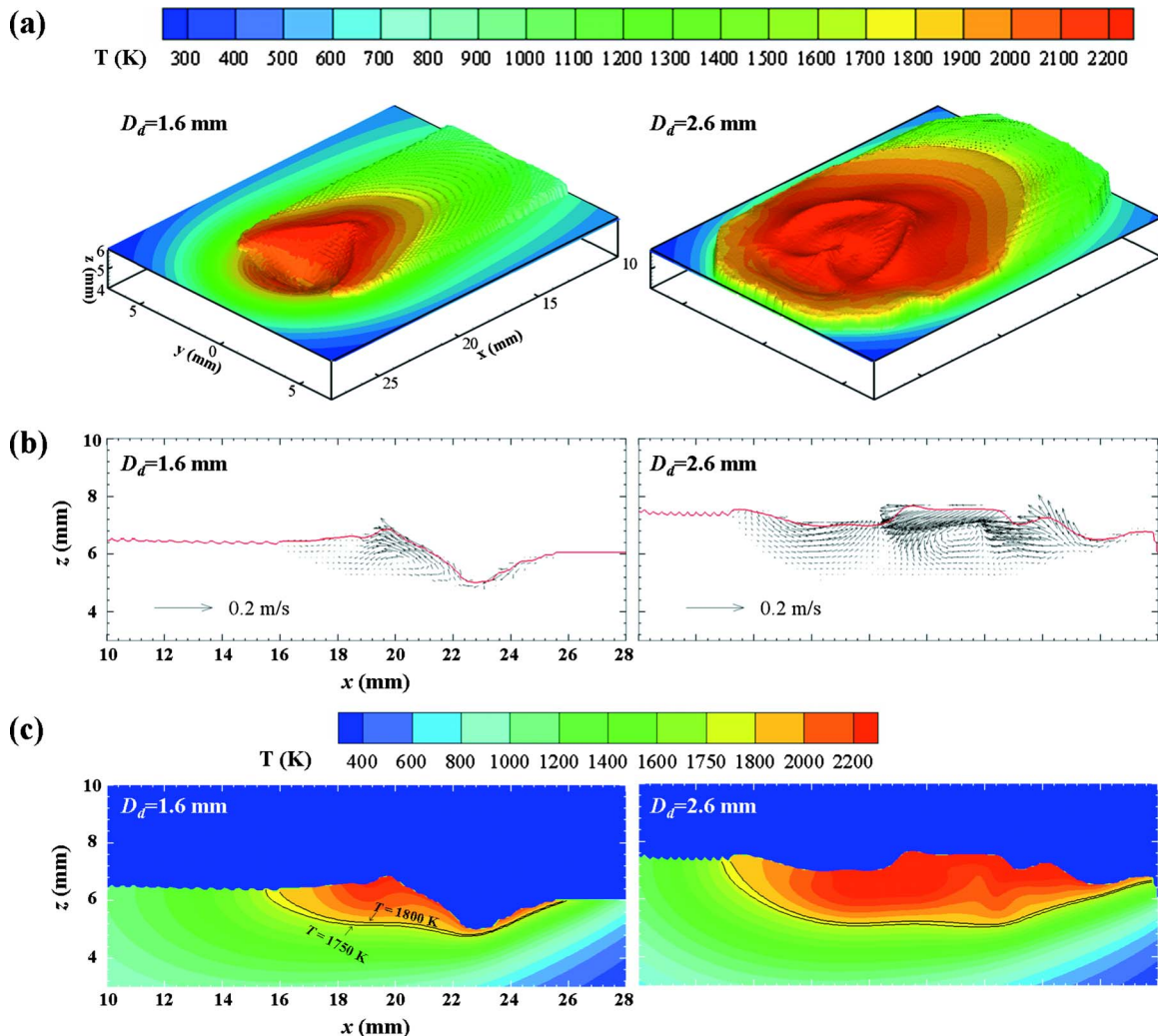


FIG. 5. (Color online) The effect of droplet size: $D_d=1.6$ mm and $D_d=2.6$ mm at $t=2.0$ s; (a) 3D weld bead shapes with ripples and temperature distributions, (b) side views of velocity distributions, and (c) side views of temperature distributions; same other welding parameters: $I=240$ A, $D_f=13.8$ Hz, $D_v=-70$ cm/s, and $V_a=0.7$ cm/s.

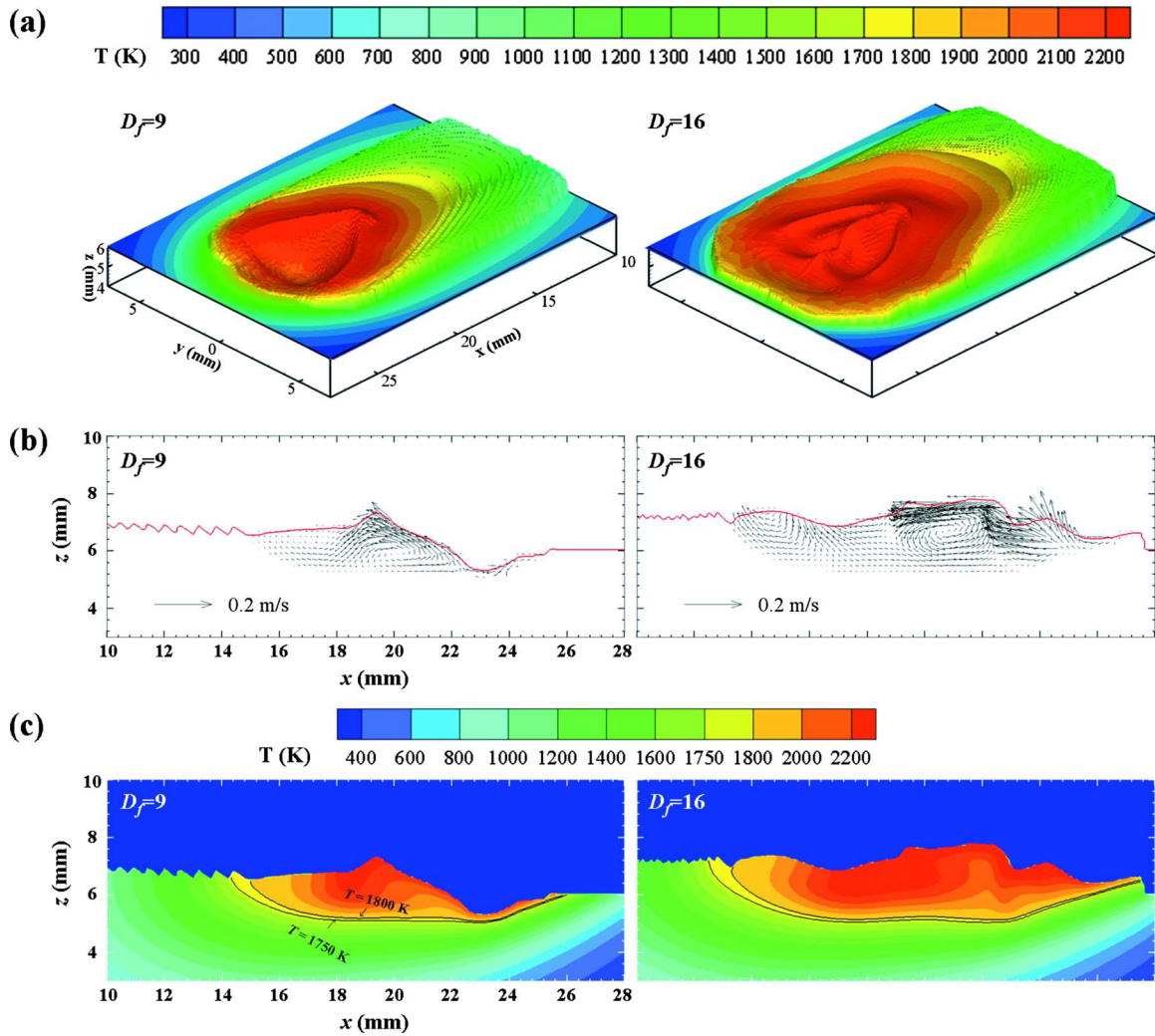


FIG. 6. (Color online) The effect of droplet frequency: $D_f=9$ Hz and $D_f=16$ Hz at $t=2.0$ s; (a) 3D weld bead shapes with ripples and temperature distributions, (b) side views of velocity distributions, and (c) side views of temperature distributions; same other welding parameters: $I=240$ A, $D_e=2.34$ mm, $D_o=-70$ cm/s, and $V_o=0.7$ cm/s.

more molten metal deposit onto the weld pool in the same duration which results in a larger weld pool and deeper weld penetration.

As shown in Table II, for lower welding currents ($I=220$ and 240 A), the droplet diameters are much larger than the electrode diameter (1.6 mm), and the droplet frequency is relatively low (below 20 Hz). The metal transfer mode is globular and the ripples on the solidified weld bead have arc-shaped features and are fairly uniform in appearance and spacing. As welding current increases, the globular mode will become spray mode. For example, at $I=280$ A, the metal transfer falls in the spray regime which is characterized by small droplets with very high droplet frequencies.¹ At $I=260$ A, the metal transfer model is still globular but close to the spray mode. Figure 4 shows that the pitch and the height of the ripples are strongly dependent on the welding current. For $I=220$, 240, and 260 A, the average pitches of the ripples are, respectively, about 0.60, 0.37, and 0.26 mm, and the corresponding heights are, respectively, about 0.21, 0.18, and 0.12 mm. It is found that for these three current levels, the ripple pitch is inversely proportional to the droplet frequency ($D_f=8.8$, 13.8, and 23.8 Hz, respectively).

Hence, a higher current corresponds to a higher droplet frequency and a smaller droplet size, which leads to denser and smaller ripples on the weld bead. The results are consistent with the previous discussion that droplet impingement is the main reason for the periodic up-and-down of the weld pool which can significantly affect the ripple formation.

At $I=280$ A, the droplet frequency is 59 Hz and the droplet diameter is 1.62 mm which is close to the electrode diameter of 1.6 mm. As shown in Figs. 3 and 4, the ripples are quite fine and irregular and the maximum height is estimated to be about 0.04 mm. Note the heights of the ripples exceed the resolution of the grid size in the calculation which is 0.1 mm. Although the grid size can be further fined, it will significantly increase the calculation time. For all cases shown in Fig. 4(b), it is observed that a higher current level corresponds to a higher temperature gradient and a narrower mushy zone near the tail edge of the weld pool. The length of the solidified weld bead is shorter for the higher current level which indicates a slower solidification rate. The decrease in solidification rate allows more time for the weld pool near the tail edge to level off, leading to the ripples with less height. In addition, the smaller droplets coupling with a

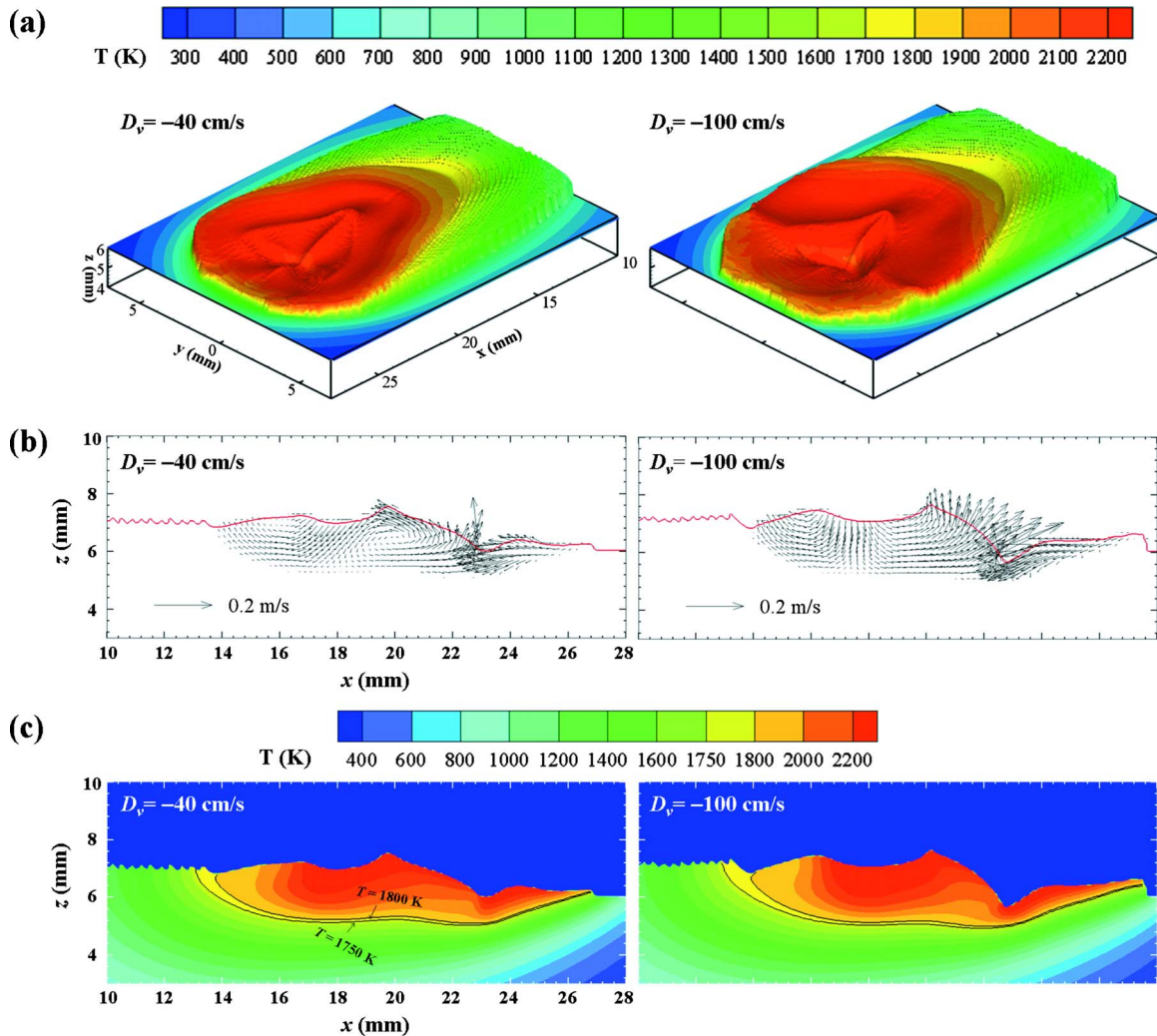


FIG. 7. (Color online) The effect of droplet impinging velocity: $D_v = -40$ m/s and $D_v = -100$ m/s at $t = 2.0$ s; (a) 3D weld bead shapes with ripples and temperature distributions, (b) side views of velocity distributions, and (c) side views of temperature distributions; same other welding parameters: $I = 240$ A, $D_d = 2.34$ mm, $D_f = 13.8$ Hz, and $V_a = 0.7$ cm/s.

larger weld pool results in a smaller extent of up-and-down of the weld pool, which decreases the ripple height. From the above discussion, the ripple shape, pitch, and height, can be attributed to the droplet impinging parameters, including the droplet size, droplet frequency, and droplet impinging velocity, which are further studied below.

C. The effect of droplet parameters

As discussed above, the final appearance of the ripple strongly depends on the up-and-down of the weld pool and the solidification rate which are closely related to the droplet impinging parameters, including the droplet size, droplet frequency, and droplet impinging velocity. In the following, a parametric study is conducted to examine the effect of each droplet impinging parameter on the weld pool transport phenomena and the subsequent ripple formation. Based on the experimental data for $I = 240$ A,³⁰ several droplet parameters are selected for this parametric study as shown in Table III. The Case I and II are used to study the effect of droplet diameter; Case III and IV are for droplet frequency; and Case V and VI are for droplet impinging velocity. The parametric study provides fundamental understanding to the role that

each of these parameters plays on the ripple formation. Note the droplet parameters are significantly coupled with the welding conditions and it may not be able to isolate one parameter from the others in practice. Recently, however, the pulsed-current GMAW process can control and achieve the desired droplet size and droplet frequency at a lower average current which, therefore, changes the inherent relation between the welding current and droplet generation that exists in the conventional GMAW process.

Figure 5 shows the effect of droplet size on the temperature and fluid flow distributions, weld pool geometries, and surface ripples on the solidified weld beads; while other welding parameters remain the same (Case I and II). It is clearly seen, the larger droplet size creates a larger weld pool, a larger weld bead, and deeper weld penetration. This is understandable because more molten metal deposits onto the workpiece in the same duration for larger droplets. Also, a more complex flow in the weld pool is found for larger droplets. As shown in Fig. 5(b), the length of the solidified weld bead is longer for smaller droplets which implies a higher solidification rate for $D_d = 1.6$ mm. The average pitch for $D_d = 1.6$ mm is about 0.47 mm, and is about 0.37 mm for

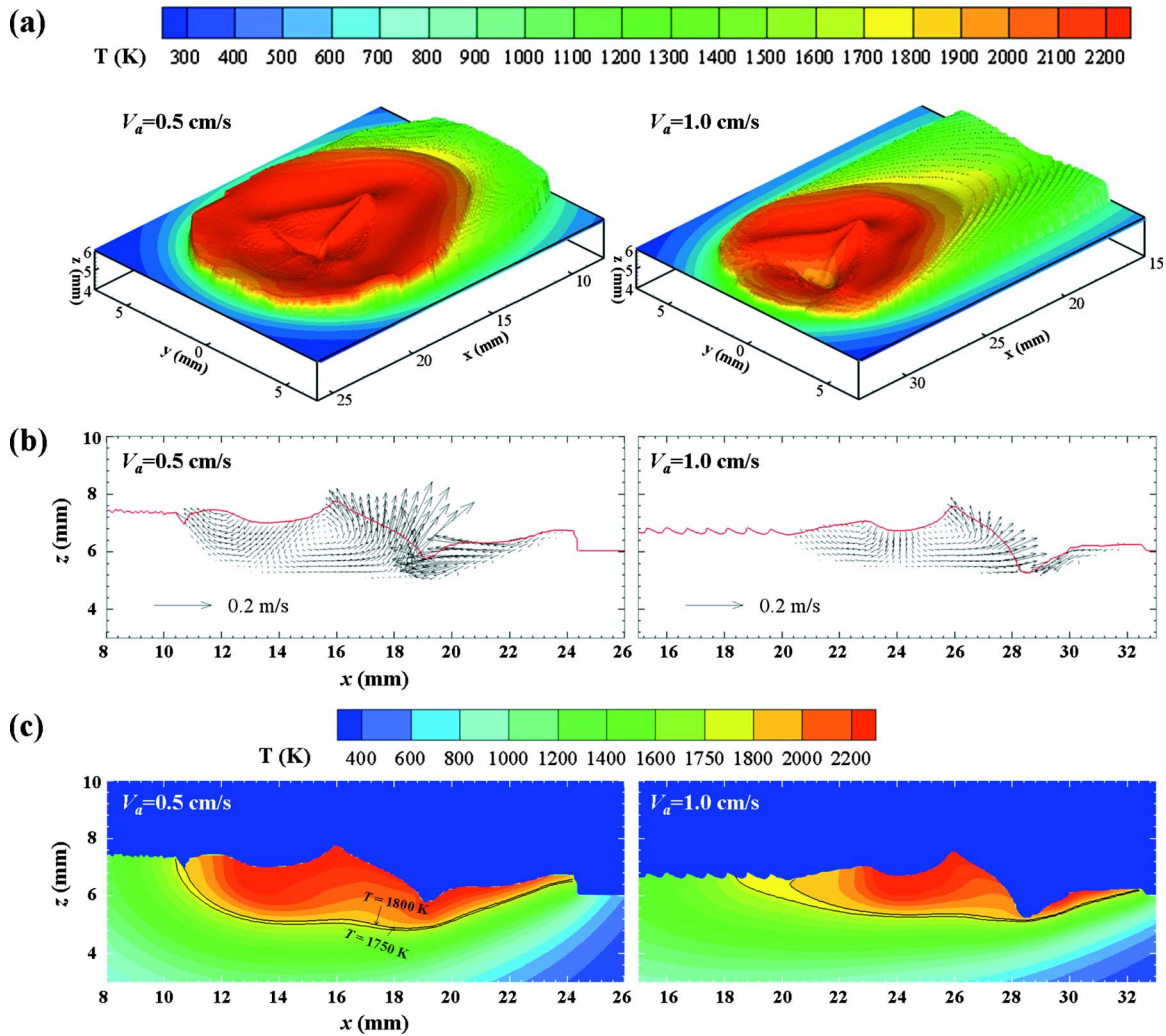


FIG. 8. (Color online) The effect of travel velocity: $V_a = 0.5$ cm/s and $V_a = 1.0$ cm/s at $t = 2.0$ s; (a) 3D weld bead shapes with ripples and temperature distributions, (b) side views of velocity distributions, and (c) side views of temperature distributions; same other welding parameters: $I = 240$ A, $D_d = 2.34$ mm, $D_f = 13.8$ Hz, and $D_v = -70$ cm/s.

$D_d = 2.6$ mm. Hence, the smaller droplet size leads to a higher solidification rate, a smaller weld pool, and a larger ripple pitch. It is seen the tip of the ripple is sharper for larger droplets but there is not much difference on the height of the tip between the two droplet diameters.

Figure 6 shows the effect of droplet frequency on the temperature and fluid flow distributions in the weld pool, weld bead geometries, and surface ripples; while the other welding parameters remain the same (Case III and IV). Apparently, for a higher droplet frequency, more droplets deposit onto the workpiece per unit time and a larger weld pool is created, leading to a stronger convection and mixing in the weld pool. The average pitches for $D_f = 9$, 13.8 (Fig. 2), and 16 Hz are, respectively, about 0.6, 0.37, and 0.28 mm. Hence, a higher droplet frequency generates a finer pitch of ripples. It is also seen that the solidification rate in the welding direction and the height of the pitch are greater for the lower droplet frequency. Hence, the less droplet frequency leads to a higher solidification rate, a smaller weld pool, a greater ripple pitch, and a larger ripple height.

The effect of droplet impinging velocity on the temperature and velocity distributions in the weld pool, weld bead

geometries, and surface ripples are given in Fig. 7 (Case V and VI). As shown in Fig. 7, although the higher impinging velocity creates a larger weld pool, the increase in the weld pool size and weld penetration depth are not proportional to the increase in the impinging speed ($D_v = -100$ cm/s versus $D_v = -40$ cm/s). This is partially because the momentum of the high impinging droplet is damped out by the weld pool. It appears the pitch and height of the ripple and the solidification rate do not significantly depend on the droplet impinging velocity.

D. The effect of travel speed

Figure 8 shows the effect of welding travel speed on the weld bead shape and temperature and velocity distributions in the weld pool. While the other welding conditions remain the same as those at $I = 240$ A given in Table II, a higher travel speed implies less arc heat flux and fewer droplets impinge onto a unit length of the workpiece. Hence, at a lower travel speed, $V_a = 0.5$ cm/s, a larger weld pool and a larger solidified weld bead (thickness and width) with deeper weld penetration are created as compared to $V_a = 1.0$ cm/s. It

is seen the height (or thickness) of the weld bead above the original thickness of the base metal (which is 6 mm) is about 1.40 mm for $V_a=0.5$ cm/s, while it is only about 0.72 mm for $V_a=1.0$ cm/s. However, the ripples are much larger in both the pitch between two ripples and the height of the ripple's tip for $V_a=1.0$ cm/s as compared to the lower travel speed $V_a=0.5$ cm/s. As more droplets impinge onto the weld pool per unit length of the workpiece, the pitch between two ripples decreases for a slower travel speed. For a higher travel speed, due to less thermal energy (from both the droplets and the arc heat flux) is deposited onto the workpiece, the solidification rate in the welding direction is higher as compared to a lower travel speed. Also, for a higher travel speed, as there is less time for fluid convection and mixing in the weld pool, the thermal gradient near the tail edge of the weld pool significantly decreases and the size of the mushy zone increases, Fig. 8(c). In a lower travel speed, the solidification rate is lower, and the droplet impinging momentum tends to be damped out by the larger weld pool. As a result, there is more time for the up-and-down weld pool to "level off" itself near the tail edge of the weld pool which leads to much smaller pitch and height of the ripple, as compared to the higher travel speed.

V. CONCLUSIONS

The influence of welding conditions, including the welding current, droplet impingement, and travel speed on the formation and final appearance of ripples for a moving GMAW are numerically studied. The transient distributions of the melt flow velocity, temperature, and species in the workpiece, as well as the weld pool dynamics and surface rippling on the solidified weld bead are calculated. The sequence of the ripple formation is presented, which is found to be related to the periodic impingement of droplets, the up-and-down of the weld pool, and the solidification process. The pitch of the ripple is inversely proportional to the droplet frequency and droplet size and proportional to the travel speed; while the height of the ripple depends on the magnitude of the weld pool up-and-down (which is closely related to the droplet size and weld pool size) and the rate of solidification. The larger droplet frequency tends to decrease the solidification rate and thus the height of the ripples is reduced, while impinging velocity has a less influence. At the high welding current, the impingement of small droplets with very high frequency together with the high arc heating increase the weld pool size and penetration depth, leading to

the strong weld pool convection and reduced slow solidification rate with the result of forming lower and denser ripples. As the current is higher than the transition current, the formation of ripple may subject to a more continuous solidification growth. A slow travel speed is helpful to reduce the ripple heights but also at the risk of the reduced effective penetration.

- ¹R. L. O'Brien, *Welding Handbook*, 8th ed. (American Welding Society, Miami, 1991), Vol. 2.
- ²D. L. Cheever and D. G. Howden, *Weld. J.* (Miami, FL, U.S.) **48**, 179s (1969).
- ³D. J. Kotechi, D. L. Cheever, and D. G. Howden, *Weld. J.* (Miami, FL, U.S.) **51**, 386s (1972).
- ⁴K. Nakane, *Mem. Sch. Sci. Eng. Waseda Univ.* **44**, 1 (1980).
- ⁵A. C. Hall and C. V. Robino, *Sci. Technol. Weld. Joining* **9**, 103 (2004).
- ⁶J. Hu, H. Guo, and H. L. Tsai, *Int. J. Heat Mass Transfer* **51**, 2537 (2008).
- ⁷G. M. Oreper and J. Szekely, *J. Fluid Mech.* **147**, 53 (1984).
- ⁸M. Kanouff and R. Greif, *Int. J. Heat Mass Transfer* **35**, 967 (1992).
- ⁹Y. H. Xiao and G. D. Ouden, *Weld. J.* (Miami, FL, U.S.) **72**, 428s (1993).
- ¹⁰P. Dutta, Y. Joshi, and R. Janaswami, *Numer. Heat Transfer, Part A* **27**, 499 (1995).
- ¹¹N. Chakraborty, S. Chakraborty, and P. Dutta, *Numer. Heat Transfer, Part A* **45**, 391 (2004).
- ¹²J. W. Kim and S. J. Na, *ASME J. Eng. Ind.* **116**, 78 (1994).
- ¹³M. Ushio and C. S. Wu, *Metall. Mater. Trans. B* **28B**, 509 (1997).
- ¹⁴S. Ohring and H. J. Lugt, *Weld. J.* (Miami, FL, U.S.) **79**, 416s (2000).
- ¹⁵Z. Cao, Z. Yang, and X. L. Chen, *Weld. J.* (Miami, FL, U.S.) **83**, 169s (2004).
- ¹⁶M. C. Tsao and C. S. Wu, *Weld. J.* (Miami, FL, U.S.) **67**, 70s (1988).
- ¹⁷J. Jaidi and P. Dutta, *Numer. Heat Transfer, Part A* **40**, 543 (2001).
- ¹⁸Y. Wang, Q. Shi, and H. L. Tsai, *Metall. Mater. Trans. B* **32B**, 145 (2001).
- ¹⁹Y. Wang and H. L. Tsai, *Int. J. Heat Mass Transfer* **44**, 2067 (2001).
- ²⁰Y. Wang and H. L. Tsai, *Metall. Mater. Trans. B* **32B**, 501 (2001).
- ²¹H. G. Fan and R. Kovacevic, *J. Phys. D* **37**, 2531 (2004).
- ²²H. G. Fan and R. Kovacevic, *Metall. Mater. Trans. B* **30B**, 791 (1999).
- ²³F. L. Zhu, H. L. Tsai, S. P. Marin, and P. C. Wang, *Prog. Comput. Fluid Dyn.* **4**, 99 (2004).
- ²⁴J. Hu and H. L. Tsai, *Int. J. Heat Mass Transfer* **50**, 833 (2007).
- ²⁵J. Hu and H. L. Tsai, *Int. J. Heat Mass Transfer* **50**, 808 (2007).
- ²⁶J. Hu and H. L. Tsai, *J. Appl. Phys.* **100**, 053304 (2006).
- ²⁷J. Hu and H. L. Tsai, *ASME J. Heat Transfer* **129**, 1025 (2007).
- ²⁸D. B. Kothe and R. C. Mjolsness, Los Alamos Report No. LA-UR-91-2818, 1991.
- ²⁹Q. Z. Diao and H. L. Tsai, *Metall. Trans. A* **24**, 963 (1993).
- ³⁰L. A. Jones, T. W. Eagar, and J. H. Lang, *J. Phys. D* **31**, 107 (1998).
- ³¹P. C. Carman, *Trans. Inst. Chem. Eng.* **15**, 150 (1937).
- ³²S. Minakawa, I. V. Samarasekera, and F. Weinberg, *Metall. Trans. B* **16**, 823 (1985).
- ³³G. S. Beavers and E. M. Sparrow, *ASME J. Appl. Mech.* **36**, 711 (1969).
- ³⁴P. Sahoo, T. Debroy, and M. J. McNallan, *Metall. Trans. B* **19**, 483 (1988).
- ³⁵T. Zacharia, S. A. David, and J. M. Vitek, *Metall. Trans. B* **22**, 233 (1991).
- ³⁶J. E. Welch, F. H. Harlow, J. P. Shannon, and B. J. Daly, Los Alamos Report No. LA-3425, 1966.
- ³⁷M. D. Torrey, L. D. Cloutman, R. C. Mjolsness, and C. W. Hirt, Los Alamos Report No. LA-10612-MS, 1985.